IEEE Photonics Journal
An IEEE Photonics Society Publication

Open Access

Polarimetric Identification of 3D-Printed Nano Particle Encoded Optical Codes

Volume 12, Number 3, June 2020

Kavan Ahmadi
Pedro Latorre-Carmona
Bahram Javidi, *Fellow, IEEE*
Artur Carnicer

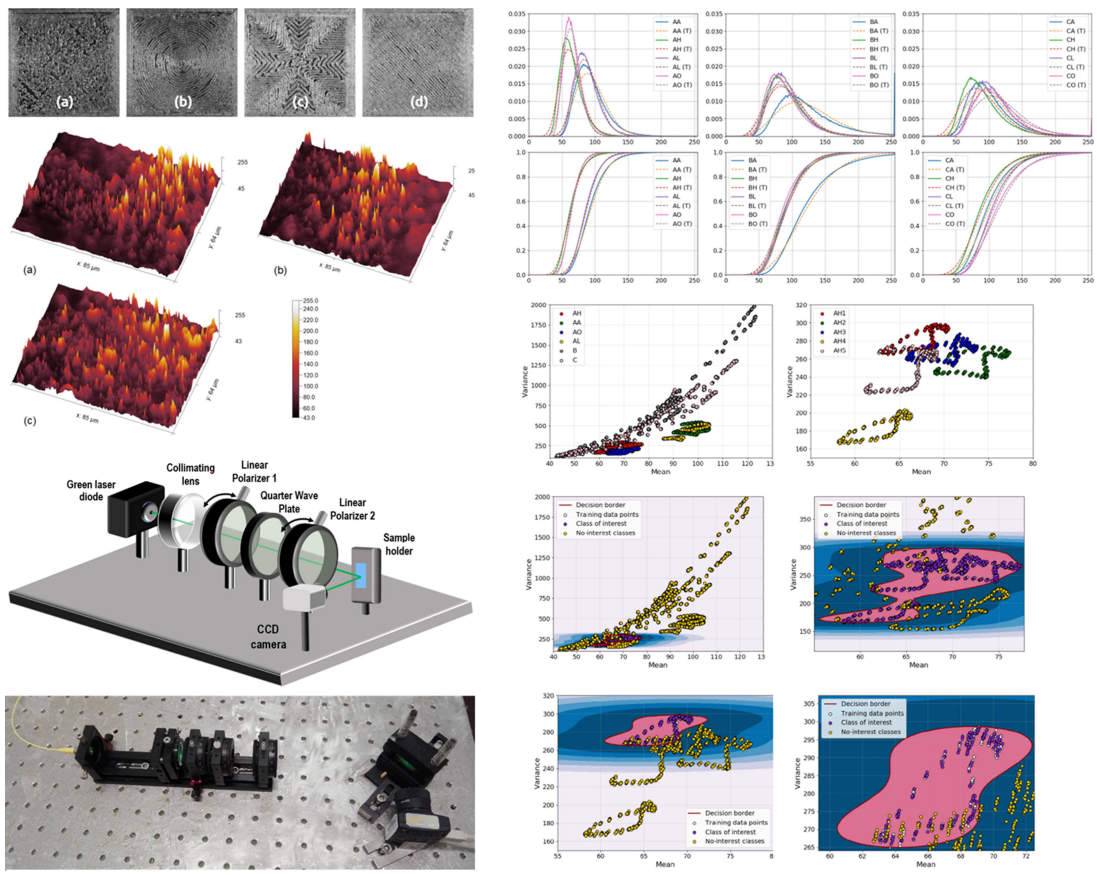

DOI: 10.1109/JPHOT.2020.2987484

Polarimetric Identification of 3D-Printed Nano Particle Encoded Optical Codes

Kavan Ahmadi,[1] Pedro Latorre-Carmona ,[2] Bahram Javidi ,[3] *Fellow, IEEE*, and Artur Carnicer [1]

[1]Departament de Física Aplicada, Facultat de Física, Universitat de Barcelona (UB), 08028 Barcelona, Spain
[2]Departamento de Ingeniería Informática, Universidad de Burgos, 09006 Burgos, Spain
[3]Department of Electrical and Computer Engineering, University of Connecticut, Storrs, CT 06269-4157 USA

DOI:10.1109/JPHOT.2020.2987484

Manuscript received March 9, 2020; revised April 5, 2020; accepted April 8, 2020. Date of publication April 16, 2020; date of current version May 26, 2020. Bahram Javidi acknowledges support in part by Air Force Office of Scientific Research (AFOSR) FA9550-18-1-0338. The work of Artur Carnicer was supported by Ministerio de Economía y Competitividad (MINECO) under Grant FIS2016-75147-C3-1-P.
Corresponding author: Artur Carnicer (email: artur.carnicer@ub.edu).

Abstract: Document signature is a powerful technique used to determine whether a message is tampered or valid. Recently, this concept was extended to optical codes: we demonstrated that the combined use of optical techniques and machine learning algorithms might be able to distinguish among different classes of samples. In the present work, we produce nano particle encoded optical codes with predetermined designs synthesized with a 3D printer. We used conventional polylactic acid filament filled with metallic powder to include the effect of nano-encoding for unique polarimetric signatures. We investigated an interesting real-world scenario, that is, we demonstrate how a single class of codes is distinguished among a group of samples to be rejected. This is a difficult unbalanced problem since the number of polarimetric signatures that characterize the true class is small compared to the complete dataset. Each sample is characterized by analyzing the polarization state of the emerging light. Using the one class-support vector machine algorithm we found high accuracy figures in the recognition of the true class codes. To the best of our knowledge, this is the first report on implementing optical codes with nano particle encoded materials using 3D printing technology.

Index Terms: Optical authentication and security, optical polarization, speckle noise.

1. Introduction

The application of optical technologies and methods for security verification and encryption is becoming an active research area [1], [2]. In fact, optical authentication can be arguably considered as a well-established research field (see [3] for a comprehensive tutorial on this topic). In particular, photonics devices produced with metamaterials will play a key role in optical security technology [4]. The polarimetric signature is one of the properties that has been used to authenticate and classify samples. In [5], authors showed that Quick Response (QR) codes made with metallic nanoparticles can be authenticated with a high rate of success. Nanoparticles convert the QR codes into polarimetric sensitive materials, and its corresponding signature is used as a feature vector for classification. QR codes produced using standard thin-film technology can be classified (distinguished) analyzing the polarimetric properties of the reflected light (in particular, using

a Mueller matrix image ellipsometer) [6]. The polarimetric response has also been used as a discernible feature in other fields, like the pharmaceutic industry sector, where pharmaceutical pills were coated with gold nanoparticles. In this case, a four-PEM Mueller matrix polarimeter was used to characterize the polarimetric response of the samples [7]. All the above mentioned problems have a distinctive feature: the number of samples produced is highly restrictive due to the production costs associated to this type of technologies.

Three-dimensional printing can be understood as any group of processes by which some materials are joined or solidified through a computer controlled system, in order to create a three-dimensional object. 3D printers can be used to print different types of structures using a relatively large number of materials and with different types of filling patterns. In particular, 3D printing allows us to create a relatively large number of samples of different classes. However, this technology depends on its building orientation because this orientation has a direct effect on the microstructure and the mechanical properties of each 3D production. Moreover, its effect is not controllable, or even predictable [8]–[11]. In particular, 3D printers might print identical samples with different microstructures and mechanical properties, and therefore, they can be used as Physical Unclonable Functions materials, in which this physical structure is hard to predict [12], [13].

In this paper, we demonstrate the synthesis and fabrication of nano particle encoded optical codes fabricated with a 3D printer. This approach can substantially simplify the transition of optical techniques for security authentication for practical applications. In the experiments, we discuss the classification of a single class of codes and how the 3D printed code can be distinguished from a group of samples to be rejected. Experimental results and theoretical analysis verify the feasibility of the proposed approach. The samples in the experiments were created using commercially accessible materials and low-cost technology. In particular, we used polylactic acid (PLA), which is a particular type of plastic material used in 3D printing, combined with metallic powder. The codes produced in this way display polarimetric signatures similar to those generated by samples made of metallic nanoparticles or thin film structures. On the other hand, we set out this problem as a highly unbalanced, one-class pattern recognition classification problem, in the sense that the system should be able to distinguish just one type of 3D printed structure. The total number of samples of this class of interest is relatively small as compared to the total amount of samples with different materials that we could classify.

The paper is organized as follows: Section 2 presents the synthesis of the optical codes, and the optical acquisition set-up used to obtain the polarization signatures from each sample. These polarimetric signatures are the particular features that are used for the classification stage. Section 3 describes the main properties of One-Class Classifiers based on Support Vector Machines used in pattern classification in unbalanced classification scenarios. Section 4 presents the results corresponding to the two one-class classification problems we aim at solving. The main conclusions are presented in Section 5.

2. Design of Samples, Experimental Set-Up and Feature Extraction Process

We produced $20 \times 20 \times 2$ mm^3 sample codes using an inexpensive Anet A8 DIY 3D printer. On one face of the sample we placed QR codes (or other encoded data) with the required information, whereas the other side is used for authentication purposes. As mentioned in the previous section, the structures were produced using PLA filament filled with metallic (or metallic alloys) powder. In particular, we used PLA filled with aluminum, brass and copper (AptoFun wire, produced by Aptotec UG, Tübingen, Germany). The reverse of the samples is expected to be a flat surface produced using four different filling algorithms: Hilbert, Archimedean, octagram and rectilinear. Fig. 1 shows four samples made of aluminum PLA and the four filling procedures: (i) the Hilbert procedure provides a random irregular look, (ii) the Archimedean algorithm fills the surface with concentric circles, (iii) the octogram approach provides a Malta cross look whereas (iv) the rectilinear method fills the surface using parallel lines. It is quite apparent (see Fig. 1) that the amount of details in the sample depends on the selected filling method: for instance, rectilinear and Archimedian procedures produce more dense patterns compared to the octagram

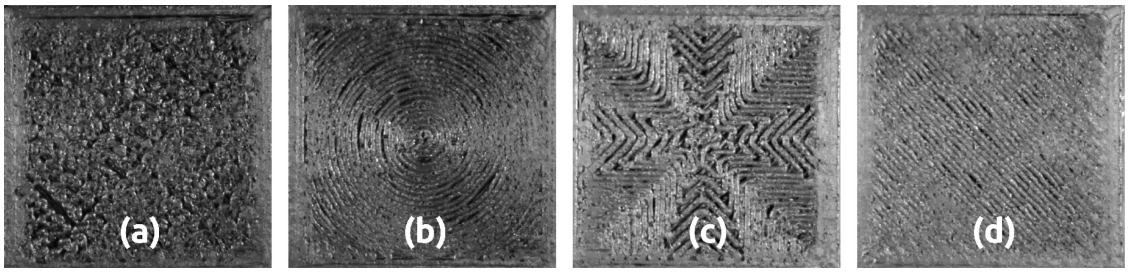

Fig. 1. Samples: (a) Aluminum PLA - Hilbert, (b) Aluminum PLA - Archimedean, (c) Aluminum PLA - Octagram and (d) Aluminum PLA - Rectilinear. The size of the samples is 20 $\times$ 20 $\times$ 2 mm^3.

TABLE 1
Produced Samples. The Number and the Parenthesis Indicate How Many Samples of this Class Were Produced and How the Classes are Labeled, Respectively

	Archimedian	Hilbert	Rectilinear	Octagram
Aluminum - PLA	2 (AA)	5 (AH)	2 (AL)	2 (AO)
Brass - PLA	1 (BA)	1 (BH)	1 (BL)	1 (BO)
Copper - PLA	1 (CA)	1 (CH)	1 (CL)	1 (CO)

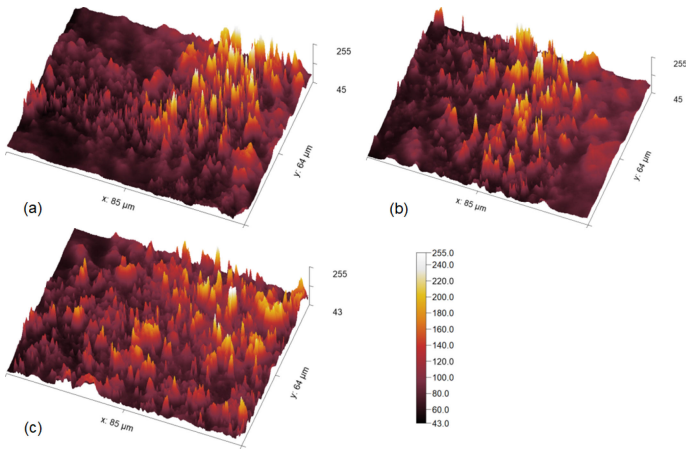

Fig. 2. Confocal microscope images: (a) Aluminum; (b) Brass (c) Copper. The size is 85 μm $\times$ 64 μm and the peak-to-valley depth is 25 μm (elevation values range from 43 to 255).

template. A description of the printing algorithms used can be found elsewhere. See, for instance, [14]. Combining the three different PLA filaments and filling algorithms we were able to produce 12 different classes of samples. The experiment was carried out using a total of 19 samples according to Table 1. The printing variables (bed and nozzle temperatures, the filling pattern density, the diameter of the filaments and the 3D printer extrusion type) were kept constant for all the samples. We used the following printing parameters: Fill pattern density: 5%; nozzle temperature: 190° C; bed temperature: 50 $^\circ$C; filament diameter: 1.75 mm; layer height: 0.3 mm.

The manufacturer of the filaments does not provide any information of the characteristics of the metallic powder used in the fabrication of the PLA wire. In order to provide more insight on this issue, we show confocal microscope images of three samples made of aluminum, copper and brass (Fig. 2(a)-(c)). The instrument used was a Sensorfar PLμ 200 microscope with a 150$\times$ NA $=$ 0.95 Nikon objective. The size of the images is 770 $\times$ 576 pixels corresponding to an area of 85 μm $\times$ 64 μm with a pixel depth of 8 bits; the resolution depth of the instrument is 25 μm with elevation values ranging from 43 to 255. Note that the topography of the samples is irregular and does not follow any pattern.

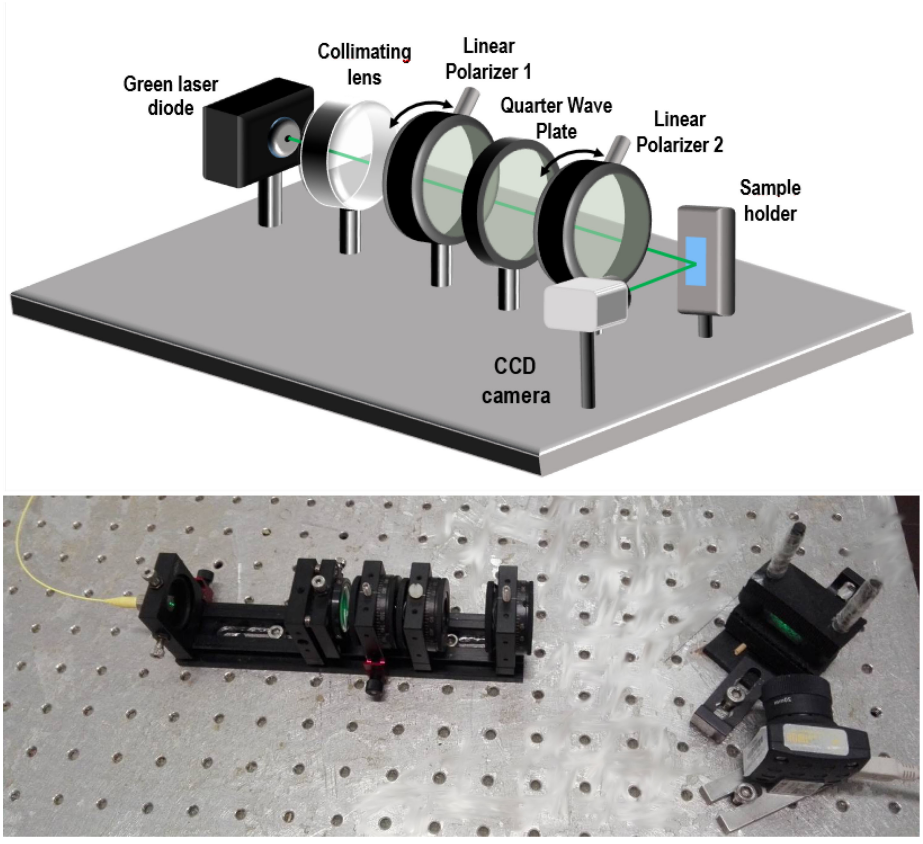

Fig. 3. Experimental setup

Fig. 3 shows a sketch of the optical set-up used to measure the polarimetric signatures given by the different metallic materials. A green laser diode emitting at $\lambda = 532$ nm, passes through a collimation lens, a linear polarizer and a quarter wave plate. This allows to generate a circularly polarized output beam. Then, this beam finally meets another linear polarizer. The output light meets the sample, and the speckle pattern produced is acquired by an 8-bit CCD camera. The second linear polarizer defines the polarization direction of the incident beam. The angle of the polarizer was changed from 0 to 175° in steps of 5°. For each polarization direction, 10 images were acquired with the CCD camera, i.e., 360 speckle patterns which are reflected from the surface of each 3D printed sample. Then, the histogram for every speckle image is assessed. Note that the sample is placed at 55° with respect to the optical axis (which corresponds to the Brewster angle of PLA with refractive index $n_d = 1.465$ [15]). The sample is set at this particular angle because the strongest dependence of the reflected intensity as a function of the direction of polarization of the incident beam can be found.

Fig. 4(a) shows recorded speckle images corresponding to AA, BA and CA samples (see Table 1 for nomenclature). Fig. 5 displays the histograms and cumulative histograms (normalized to the number of pixels) calculated from a speckle image for one sample of the 12 classes. In all the depicted cases, the direction of the second polarizer is set to 0°. According to the shape of these curves, the statistics of the recorded images are compatible with a Gamma Probability Distribution [16]:

$$P(g) = \left(\frac{n_0}{\bar{g}}\right)^{n_0} \frac{g^{n_0-1}\exp(-gn_o/\bar{g})}{\Gamma(n_0)} \quad \text{and} \quad n_0 = \left(\frac{\bar{g}}{\sigma}\right)^2 \tag{1}$$

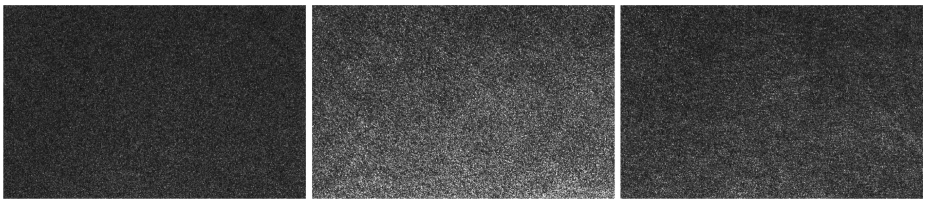

Fig. 4. Recorded speckle images for one sample of classes AA (left), BA (center) and CA (right). In the three cases the second polarizer is set to 0°.

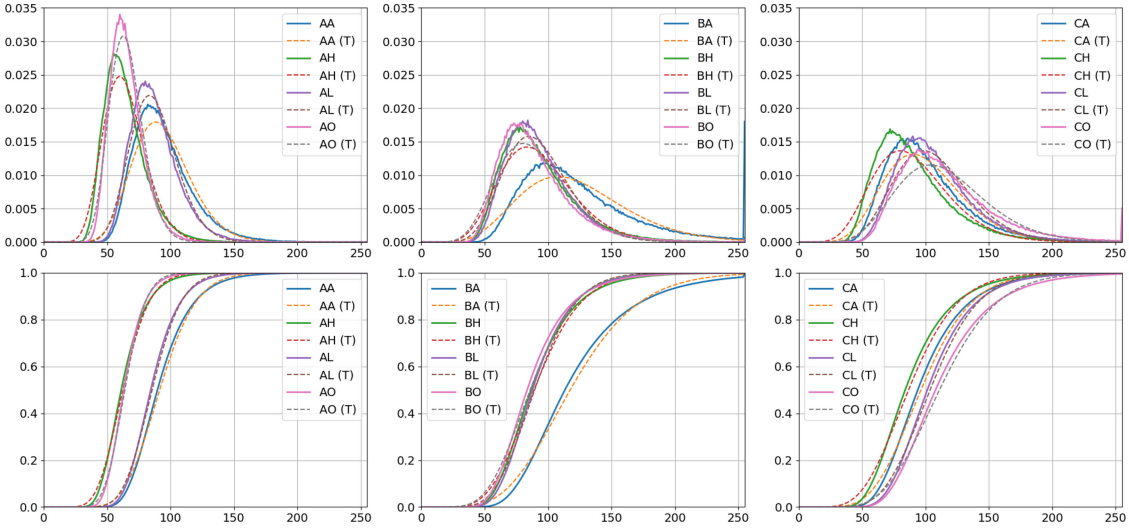

Fig. 5. First row: Probability Density Function for one example of each class of printed codes at 0° of incident polarization direction as a function of gray level g. The curves labeled with (T) denote the theoretical estimation, according to $P(g)$ [Eq. (1)]. Left: aluminum, center: brass, right: copper. Second row: Corresponding cumulative histograms. See Table 1 for the definition of abbreviations.

where g is the corresponding gray level and $\bar{g}$ and σ are the mean and the standard deviation of the experimental recorded image; $\Gamma()$ stands for the Gamma function. We also displayed $P(g)$ on Fig. 5 (see dotted line curves, labeled with '(T)' in the legend). Interestingly, the $P(g)$ distributions approximately reproduce the experimental histograms. This fact is confirmed when the cumulative histograms are analyzed (see second row of Fig. 5).

The speckle characteristics of the reflected beam strongly depend on the direction of polarization of the incident light. According to the Fresnel formulae, p- and s- polarization depend on the angle of incidence and the refraction index of the sample material. Interestingly, the refractive index of the PLA samples will be slightly modified because of the presence of metallic powder with complex refractive indexes (aluminum: n $= 0.938 + 6.420i$, brass: $0.568 + 2.589i$ and copper: $1.116 + 2.596i$ [15]). Moreover, the surface of the produced samples is coarse (Fig. 1), even at the microscopic level (Fig. 2) and thus, the angle of incidence varies at each point of the surface. For this reason, each sample can be considered as unique. Fig. 6 displays how the probablity distribution is modified when Linear Polarizer 2 is rotated at the following angles: {0°, 20°, 40°, 60°, 80°}. In this figure, three samples are considered:{AH, BH, CH}.

According to these results, each experimental curve can be identified by means of the mean and the variance values (see Eq. (1)). These two features define the so-called feature vector that will be used in the classification stage.In order to provide some insight into the behavior of the problem we plot the variance versus the mean of the experimental dataset (see Fig. 7). It is important to note that each data point that appears in Fig. 7 represents a particular feature vector. This feature

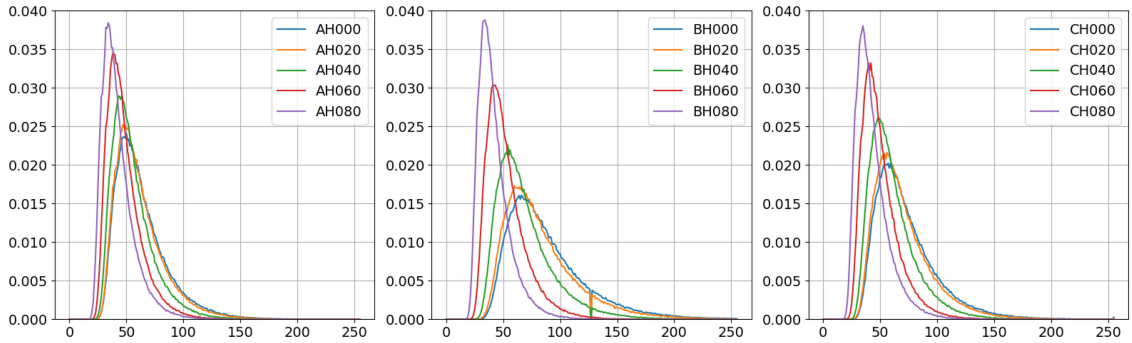

Fig. 6. Probability Density Functions for one example of each class of printed codes for different directions of polarization as a function of gray level *g*. Left: AH sample, center: BH sample, right: CH sample.See Table 1 for the definition of abbreviations.

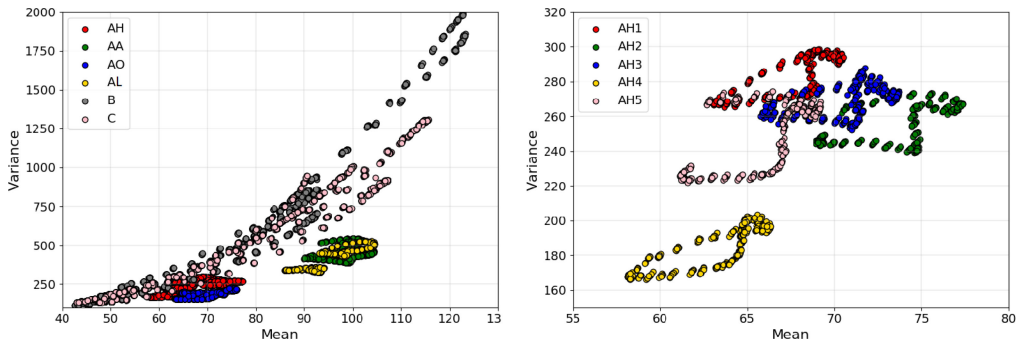

Fig. 7. Variance versus mean of the experimental recorded speckle images. Left: Complete dataset. Note that for the sake of clarity, the data corresponding to classes B and C is grouped. Right: data corresponding to the samples belonging to class AH.

vector corresponds to a particular polarization measurement of a particular printed QR material and printed architecture (design), and these data points will be the points that will be classified by the one-class support vector machine (OC–SVM) classifier. Section 3 presents this particular type of classification methodology.

3. One-Class Support Vector Machines for the Detection of the Class of Interest

Pattern recognition has been traditionally applied on binary (two) and multi (more than two) class problems. In this latter case, the classifier should be given data points from all the classes in order to train the classifier to identify them correctly. However, there are problems where there might be useful and enough information about only one of the classes. This is the reason why a new approach in pattern recognition appeared, called one-class classification.

One-class classification may be seen from two complementary perspectives: (a) from an *anomaly* detection and (b) from a *target* detection point of view. *Anomaly* detection is referred to the problem of detecting data and/or patterns that do not follow the expected behaviour. We refer them as as *outlier* data. *Target* detection is applied to identify specific data of interest (*target* data). The problem of classifying positive (*target*) cases in the absence of appropriately defined negative cases (*outliers*) has been given an increasing attention during the last few years. Several new methodologies and application fields have emerged, including: (1) industrial quality inspection using machine vision systems [17], (2) mobile authentication [18], and (3) remote sensing [19], just to cite a few examples.

There is a diverse and rich field of one-class classification methodologies. The interested reader is referred to [20] for an overview. One of the most extended strategies is the so-called one-class Support Vector Machine classifier (OCSVM). It has two main formulations. In the approach presented in [21] (also called Support Vector Domain Description, or SVDD), the goal is to find the smallest sphere containing the *target* data points. Alternatively, in [22] the idea is to find the hyperplane that separates the data from the origin with maximal margin. The approach in [22] is the one we will apply in our case.

In order to outline the mathematical description of this method, we will follow the nomenclature given in [22]. In particular, let us assume a group of training data points $\{\mathbf{x}_1, \ldots, \mathbf{x}_n\} \in \mathfrak{X}$, where n is the number of observations and $\mathfrak{X}$, a dataset. Let us also consider Φ as a feature map $\mathfrak{X} \rightarrow F$ where F should be mathematically understood as an inner product space where the inner product defined on the image of Φ can be computed by considering kernels: $k(\mathbf{x}, \mathbf{y}) = (\Phi(\mathbf{x}) \cdot \Phi(\mathbf{y}))$. The aim is to develop a function that returns a particular value in a region capturing most of the data points, and another constant value elsewhere. These values can be $+1$ and -1, respectively. As stated before, the strategy would be to map the data into the space defined by the kernel, and to separate them from the origin with the maximal margin that can be estimated. This is made solving the following quadratic constrained problem:

$$\min_{w \in F, \xi \in R^l, \rho \in R} \frac{1}{2}\|w\|^2 + \frac{1}{\nu n}\sum_i \xi_i - \rho,$$
$$(w \cdot \Phi(\mathbf{x}_i)) \geq \rho - \xi_i. \tag{2}$$

It can be shown that the decision function will be $f(\mathbf{x}) = \text{sgn}(w \cdot \Phi(\mathbf{x}) - \rho)$ and that, at the optimum, $\rho = (w \cdot \Phi(\mathbf{x}_i))$. ξ_i are called slack variables and deal with the errors that are allowed by the classification method for some of the training samples and ω and ρ are a weight vector and an offset that mathematically define the separating hyperplane in the feature space. Parameter ν in Eq. 2 is a parameter that is related to the number of training data points that are allowed to be outside of the region where the *target* data points are, and n represents the total number of training data points (the reader is referred to [22] for further details, in particular, for the precise and complete definition of the ν parameter).

One of the most important problems a pattern recognition (classification) dataset may have is that of class cardinality unbalance, defining a scenario where the number of data points of one of the classes is much lower than that of the other(s). This is particularly important in two-class classification problems. On the other hand, it is also common that the class that might interest most is the one with the lowest number of points. A clear case appears in image cancer diagnosis. The number of cancer cases is much lower than the number of non-cancer cases. The accuracy formulae used to predict the classification accuracy may fail giving high accuracy rates even for the case when most of the examples of the smallest class are wrongly classified. We are also aiming at solving an unbalanced problem in our case, because the number of data points *of interest* is much lower than the total number of points in the dataset. There are some strategies that have been developed in general unbalanced classification scenarios, in order to improve accuracy, or to gain some insight into the peculiar aspects of the problem at hand. However, none of them would be applicable in our case. (i) One of these strategies would imply collecting more data. In our particular scenario, this would mainly mean to increase the number of acquired polarization steps (between 0° and 360°). This solution would not help in our case, since the polarization change step size applied is small enough. (ii) We could also resample the dataset or generate new synthetic points, following techniques like SMOTE [23]. However, these techniques have very restrictive applicability and no clear gain. (iii) Finally, one last possibility could be to apply penalized or cost-sensitive classification methodologies as in [24]. Again, it would be necessary to introduce new parameters and/or derive a new objective function, without a clear relation to the physical problem at hand.

4. Results and Discussion

Our classification scenario considers two different situations. In the first one (Section 4.1) all the physical samples made using Aluminum were considered as part of the class *of interest*. In the second one (Section 4.2) just one physical sample of one particular material and filling pattern is considered as forming part of the class *of interest* and the aim is to distinguish this from other four (presumably) identical samples.

4.1. Classifying one Group of the Identical 3D Printed Samples Against the Other Different Samples

We use the complete set of nineteen 3D printed samples shown in Table 1. The 5 Aluminum-Hilbert samples form the class *of interest*. Using the procedure detailed in Section 2, we obtained 360 data points from each sample, corresponding to 10 speckle patterns from each one of the 36 different polarization directions (from 0 to 175°). Due to fluctuations of the illuminating laser beam, the resulting data points for the 10 repeated measurements are slightly different. Therefore, the total number of data points, considered as the combination of sample and polarization direction, for the class *of interest* is 1800 (=360 $\times$ 5).

Fig. 7 shows the distribution of all the data points obtained for each sample and polarization configuration. The feature vector considered for each point was that formed by the mean and variance of the histogram distribution, when modeled as a Gamma Probability Distribution, using Eq. 1. We can see that some of the *classes* overlap (Fig. 7, right plot). This happens in most of real classification problems.

From the total number of data points, 900 were randomly selected for the training stage. The other half of the points *of interest* and the complete group of points corresponding to the class(es) of *no interest* formed the test dataset. In particular, the number of data points for the class of *no interest* is 5040, which are obtained from fourteen different 3D printed samples.

The scikit-learn OCSVM implementation [25] was used. During the training stage, the (ν, γ) parameters of the OCSVM classifier were optimized using a standard grid search (in logarithmic scale) in the (ν, γ) feature space. In this case, γ corresponds to the width parameter associated to a Gaussian kernel function. Their values were those who gave the best classification accuracy rate on the training dataset.

The training set is formed only by data points of the class *of interest*. Therefore, the accuracy A during training was defined as: $A = \frac{(N_{tr} - N_{Errors})}{N_{tr}} \times 100$, where N_{tr} is the number of training data points and N_{Errors} is the number of points classified by OCSVM as points of the class of no interest. This accuracy measure can also be formulated as follows: $A = \frac{TP}{TP+FN} \times 100$. In this case, TP (True Positives) refers to the number of data points of the class of interest that are correctly classified, and FN (False Negatives) refers to the number of data points of the class *of interest* that are wrongly classified. We can consider that by maximizing the accuracy rate defined in this way, we are minimising the number of False Negative cases (type-II error). We must bear in mind that only data points of the class *of interest* are used during training, and therefore we do not assess the number of False Positive (FP) cases (type-I error), at this stage.

The test dataset is formed by data points *of interest* and those that are of *no interest*. In particular, the number of points of classes of *no interest* is almost an order of magnitude bigger than those *of interest*. In this situation, some measures of accuracy may fail [26], in the sense that they may give high accuracy values, even for cases when 50% or more of the data points of the class with lowest amount of points, are wrongly classified.

In order to deal with this problem, the *geometric mean of accuracies* [27], is considered in order to measure the classification quality. It is defined as $\text{gma} = \sqrt{\text{TPr} \times \text{TNr}} \times 100$ (in %). Here, $\text{TPr} = \frac{TP}{TP+FN}$ and $\text{TNr} = \frac{TN}{TN+FP}$. FP is the number of samples of *no interest* classified as samples *of interest* and, as a recall, FN is the number of samples *of interest* classified as samples of *no interest*. The classification accuracy was gma = 98.23%. In particular, TP = 889, FN = 11, TN = 4923 and FP = 117. This means the classifier only mistakenly classifies 11 feature data points corresponding to a

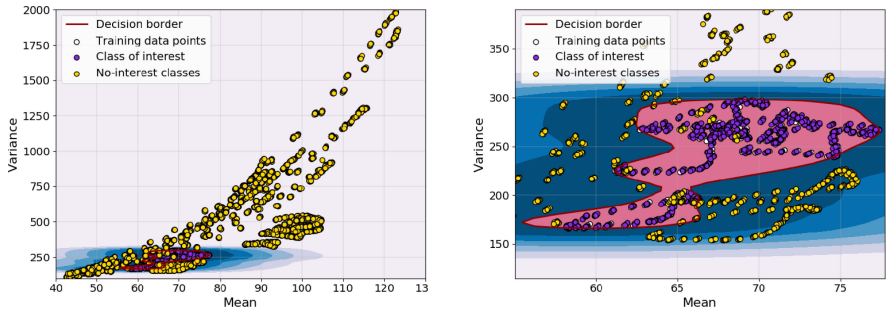

Fig. 8. Decision border given by the OC−SVM classifier for the Aluminum-Hilbert samples against the rest. A zoomed-in version is also shown for visualization purposes

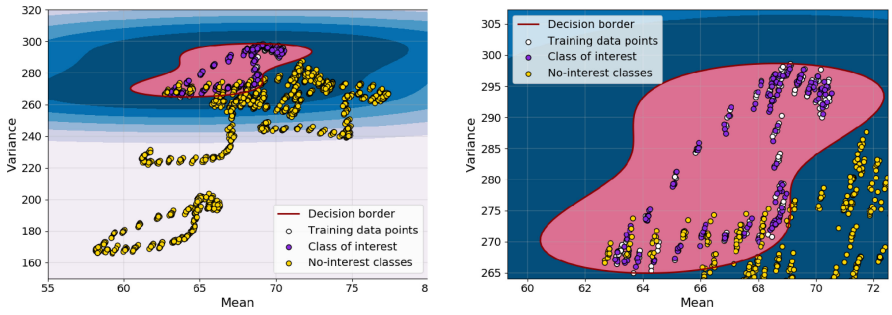

Fig. 9. Decision border given by the OC−SVM classifier for the case of one Aluminum-Hilbert sample against the other four identical samples.

class *of interest* sample as class of *no interest* out of 900, implying a high identification capability, for the class *of interest*. Fig. 8 shows the decision border given by OCSVM. A zoomed-in version of it is also shown in order to better visualize the classification result.

4.2. Classifying One Sample Against the Other Identical 3D Printed Samples

In this scenario, one Aluminum-Hilbert sample is considered as the class *of interest*, against the other four identical Aluminum-Hilbert samples. The number of sample points for the class *of interest* is 360 in this case, 180 of which are used (randomly selected) for training. On the other hand, the number of data points for the class of *no interest* is 1440, obtained from the other four Aluminum-Hilbert samples. The classification accuracy was gma $=$ 96.39%. In particular, TP $=$ 180, FN $=$ 0, TN $=$ 1338 and FP $=$ 102. This implies that no data point of the class *of interest* is wrongly classified. Fig. 9 shows the decision border given by OCSVM for the case of one Aluminum-Hilbert sample against the other four samples of the same material and printing design.

5. Conclusions

In this paper we proposed the synthesis, implementation, and classification of nano particle encoded optical codes. The nano particle encoding and fabrication of PUFs are achieved by using plastic 3D printer filaments with metallic-like powder (iron, copper or brass). The classification of the codes is carried out using polarimetric imaging based on the polarimetric signature. The classification problem is challenging in the sense that a single class of samples is distinguished among a large number of samples to be rejected. This property makes the problem unbalanced, and therefore the measured accuracy has to take this condition into account. In particular, two problems are approached: in the first one, one type of codes with printed material and printing algorithm is discriminated against a large number of other codes. In the second one, one particular sample is compared against the rest of samples. The nature of both problems is of unbalanced

type. In our experiments, not only the overall accuracy in both cases is excellent, but also the False Negative value, i.e., the number of polarimetric signatures of the code class of interest wrongly classified as class of no interest, is very low (in fact, FN = 0 in the second example), which confirms the capability of the proposed optically encoded samples with polarimetric signature approach and the classification methodology used in this particularly difficult sample distribution scenario.

Acknowledgment

The authors thank Prof. Joan Esteve (UB) for his help with the confocal microscope.

References

[1] O. Matoba, T. Nomura, E. Perez-Cabre, M. S. Millan, and B. Javidi, "Optical techniques for information security," *Proc. IEEE*, vol. 97, no. 6, pp. 1128–1148, Jun. 2009.
[2] B. Javidi *et al.*, "Roadmap on optical security," *J. Opt.*, vol. 18, no. 8, 2016, Art. no. 083001.
[3] A. Carnicer and B. Javidi, "Optical security and authentication using nanoscale and thin-film structures," *Advances Opt. Photon.*, vol. 9, pp. 218–256, 2017.
[4] S. Abdollahramezani *et al.*, "Tunable nanophotonics enabled by chalcogenide phase-change materials," 2020, *arXiv:2001.06335*.
[5] A. Carnicer, A. Hassanfiroozi, P. Latorre-Carmona, Y. P. Huang, and B. Javidi, "Security authentication using phase-encoded nanoparticle structures and polarized light," *Opt. Lett.*, vol. 40, no. 2, pp. 135–138, 2015.
[6] A. Carnicer *et al.*, "Optical security verification by synthesizing thin films with unique polarimetric signatures," *Opt. Lett.*, vol. 40, no. 22, pp. 5399–5402, 2015.
[7] A. Carnicer, O. Arteaga, J. M. Su ñé Negre, and B. Javidi, "Authentication of gold nanoparticle encoded pharmaceutical tablets using polarimetric signatures," *Opt. Lett.*, vol. 41, pp. 4507–4510, 2016.
[8] A. Pilipović, P. Raos, and M. Sercer, "Experimental testing of quality of polymer parts produced by laminated object manufacturing – LOM," *Tehnicki Vjesnik*, vol. 18, no. 2, pp. 253–260, 2011.
[9] A. Pilipović, P. Raos, and M. Sercer, "Experimental analysis of properties of materials for rapid prototyping," *Int. J. Adv. Manuf. Technol.*, vol. 40, no. 1-2, pp. 105–115, 2009.
[10] D. Dimitrov, K. Schreve, and N. D. Beer, "Advances in three dimensional printing – state of the art and future perspectives," *Rapid Prototyping J.*, vol. 12, no. 3, pp. 136–147, 2006.
[11] T. Galeta, M. Kljajin, and M. Karakasić, "Cost evaluation of shell and compact models in 3D printing," *Manuf. Eng.*, vol. 7, no. 3, pp. 27–29, 2008.
[12] R. Pappu, B. Recht, J. Taylor, and N. Gershenfeld, "Physical one-way functions," *Science*, vol. 5589, pp. 2026–2030, 2002.
[13] C. Herder, L. Ren, M. van Dijk, M. Yu, and S. Devadas, "Trapdoor computational fuzzy extractors and cryptographically–secure physical unclonable functions," *IEEE Trans. Dependable Secure Comput.*, vol. 14, no. 1, pp. 65–82, Jan./Feb. 2017.
[14] B. Akhoundi and A. Behravesh, "Effect of filling pattern on the tensile and flexural mechanical properties of FDM 3D printed products," *Exp. Mechanics*, vol. 59, no. 6, pp. 883–897, 2019.
[15] M. N. Polyanskiy, "Refractive index database," [Online]. Available: https://refractiveindex.info, Accessed on: Apr. 26, 2020.
[16] J. Dainty, "The statistics of speckle patterns," in *Progress in Optics*, vol. 14, New York, NY, USA: Elsevier, 1977, pp. 1–46.
[17] V. Chandola, A. Banerjee, and V. Kumar, "Anomaly detection: A survey," *ACM Comput. Surv.*, vol. 41, no. 3, pp. 15:1–15.58, 2009.
[18] V. M. Patel, R. Chellappa, D. Chandra, and B. Barbello, "Continuous user authentication on mobile devices: Recent progress and remaining challenges," *IEEE Signal Process. Mag.*, vol. 33, no. 4, pp. 49–61, Jul. 2016.
[19] S. Matteoli, M. Diani, and G. Corsini, "A tutorial overview of anomaly detection in hyperspectral image," *IEEE Aerosp. Electron. Syst. Mag.*, vol. 25, no. 7, pp. 5–28, Jul. 2010.
[20] S. S. Khan and M. G. Madden, "One-class classification: Taxonomy of study and review of techniques," *Knowl. Eng. Rev.*, vol. 29, no. 3, pp. 345–374, 2014.
[21] D. Tax and R. Duin, "Support vector domain description," *Pattern Recognit. Lett.*, vol. 20, pp. 1191–1199, 1999.
[22] B. Schölkopf, J. Platt, J. S. Taylor, A. Smola, and R. Williamson, "Estimating the support of a high-dimensional distribution," *Neural Comput.*, vol. 13, pp. 1443–1471, 2001.
[23] N. V. Chawla, K. W. Bowyer, L. O. Hall, and W. P. Kegelmeyer, "SMOTE: Synthetic minority over-sampling technique," *J. Artif. Intell. Res.*, vol. 16, pp. 321–357, 2002.
[24] A. Iranmehr, H. Masnadi-Shirazi, and N. Vasconcelos, "Cost-sensitive support vector machines," *Neurocomputing*, vol. 343, pp. 50–64, 2019.
[25] F. Pedregosa *et al.*, "Scikit–learn: Machine learning in python," *J. Mach. Learn. Res.*, vol. 12, pp. 2825–2830, 2011.
[26] R. Barandela, J. S. Sánchez, V. García, and E. Rangel, "Strategies for learning in class imbalance problems," *Pattern Recognit.*, vol. 36, no. 3, pp. 849–851, 2003.
[27] M. Kubat and S. Matwin, "Addressing the curse of imbalanced data sets: One sided selection," in *Proc. 14th Int. Conf. Mach. Learn.*, 1997, pp. 179–186.